

Warm deep-sea temperatures across Eocene Thermal Maximum 2 from clumped isotope thermometry

Tobias Agterhuis ¹✉, Martin Ziegler ¹, Niels J. de Winter ^{1,2} & Lucas J. Lourens ¹

The early Eocene hothouse experienced highly elevated atmospheric CO₂ levels and multiple transient global warming events, so-called hyperthermals. The deep ocean constitutes an assumed setting to estimate past global mean temperatures. However, available deep-sea temperature reconstructions from conventional benthic foraminiferal oxygen isotopes and magnesium/calcium ratios rely on uncertain assumptions of non-thermal influences, associated with seawater chemistry and species-specific physiological effects. Here we apply the carbonate clumped isotope thermometer, a proxy not governed by these uncertainties, to evaluate South Atlantic deep-sea temperatures across two hyperthermal events in the early Eocene (Eocene Thermal Maximum 2/H1 and H2; ~54 Myr ago). Our independent reconstructions indicate deep-sea temperatures of 13.5 ± 1.9 °C (95% CI) for the background conditions and average hyperthermal peak temperatures of 16.9 ± 2.3 °C (95% CI). On average, these absolute temperatures are three degrees warmer than estimates from benthic oxygen isotopes. This finding implies a necessary reassessment of (1) the Eocene seawater isotope composition and (2) pH changes in the deep ocean and its potential influence on benthic foraminiferal oxygen isotope records.

¹Department of Earth Sciences, Faculty of Geosciences, Utrecht University, Utrecht, the Netherlands. ²AMGC research group, Vrije Universiteit Brussel, Brussels, Belgium. ✉email: t.agterhuis@uu.nl

The early Eocene (56–48 Ma) was the warmest period of the Cenozoic, characterized by very high atmospheric CO₂ concentrations (≥ 1000 ppm)^{1,2}, reduced equator to pole temperature gradients, and absence of continental ice sheets^{3–6}. As such, the early Eocene hothouse is considered a potential analogue for our future climate⁷. Accurate temperature reconstructions are essential to obtain a better understanding of the functioning of the climate system under high CO₂ levels. Temperature proxy data can be used to estimate global mean temperatures and to validate the performance of model simulations of the Eocene climate^{2,8–10}. In comparison to the sea surface, the deep ocean is spatially uniform in temperature and is considered a relatively stable component in the climate system because of its high heat capacity^{11–13}. For these reasons, deep-sea temperature is commonly used to infer the state of the global climate^{7,9,14–16}.

Over the past three decades, much of our knowledge of the early Eocene climate on both long ($>10^5$ yr) and short ($<10^5$ yr) time scales has been based on deep-sea temperature estimates derived from oxygen isotope measurements of microfossil carbonate skeletons of benthic foraminifera ($\delta^{18}\text{O}_b$). For instance, negative excursions in high-resolution stable oxygen and carbon isotope records from deep marine sediments have revealed the periodic occurrence of multiple transient (10–100 kyr) episodes of global warming and ocean acidification (hyperthermal events; e.g. PETM, ETM2, and ETM3) (refs. 12,16–21), generally linked to massive release of isotopically light carbon into the ocean-atmosphere system^{4,18,22,23}.

However, the reliability of using $\delta^{18}\text{O}_b$ for temperature reconstructions is hampered by uncertainties in non-thermal factors. Besides temperature, this proxy reflects the $\delta^{18}\text{O}$ composition of the seawater ($\delta^{18}\text{O}_{\text{sw}}$), which is poorly constrained for the Earth's past^{24,25}. The traditional view is that with the absence of ice sheets in the Eocene, a fixed ice-free $\delta^{18}\text{O}_{\text{sw}}$ value can be applied to convert the $\delta^{18}\text{O}_b$ signal directly into deep-sea temperature^{12,16,26}. Yet, in this approach, other factors, such as salinity of deep water masses, are generally ignored as potential sources that could also have caused changes in $\delta^{18}\text{O}_{\text{sw}}$ (refs. 24,25). Furthermore, it is found that foraminiferal oxygen isotopes are sensitive to seawater pH and species-specific physiological factors (vital effects)^{24,25,27–30}.

In an attempt to overcome these uncertainties, estimates of early Eocene deep-sea temperatures have additionally been obtained from benthic foraminiferal magnesium/calcium (Mg/Ca) ratios^{11,31,32}. However, while this temperature proxy has the advantage of not being influenced by $\delta^{18}\text{O}_{\text{sw}}$, it depends on the Mg/Ca composition of the seawater (Mg/Ca_{sw}) (refs. 32,33). Although Mg and Ca have a conservative behaviour and are therefore equally distributed in the ocean, this Mg/Ca_{sw} ratio appears to have varied on long time scales (>1 Myr) in the past^{34,35}. Uncertainties in Mg/Ca_{sw} reconstructions and lack of sufficient understanding of the effect of these changes on foraminiferal Mg/Ca can bias temperature estimates^{32,33,36–39}. In addition, the foraminiferal incorporation of Mg and Ca is affected by the carbonate chemistry of the ocean and by vital effects that require species-specific calibrations^{36,40–44}. The dependency on other factors complicates the use of oxygen isotopes and Mg/Ca in reconstructing ocean temperature. Available deep-sea temperature reconstructions are not as robust as commonly appreciated and estimates from new proxies are hence desired.

The carbonate clumped isotope thermometer (Δ_{47}) shows potential to improve temperature reconstructions as it is insensitive to the isotope composition of the seawater^{45,46} and is largely unaffected by pH^{47–50} and physiological factors^{51–53}. This proxy uses the temperature dependence of the degree of bonding of two heavy rare isotopes (¹³C and ¹⁸O) within the carbonate

ion, with more clumping favoured at cooler temperatures^{45,46}. Recent analytical developments now ensure inter-laboratory consistency of measurements^{54,55} and allow analysis of relatively small sample sizes (e.g. foraminifera)^{56–58}. These advances in the application of the clumped isotope proxy have enabled reconstruction of marine temperatures independent from non-thermal uncertainties^{59–63}. So far, Δ_{47} -based reconstructions of the relatively cooler Miocene and middle Eocene have revealed a warmer deep ocean than traditionally accepted^{61–64}, raising the question of whether other periods in the Cenozoic also experienced warmer deep-sea temperatures than assumed.

Here we report Δ_{47} -based deep-sea temperature estimates across two early Eocene hyperthermal events, namely Eocene Thermal Maximum 2 (ETM2 or H1) and H2 that occurred ~ 2 Myr (~ 54 Ma) after the Paleocene-Eocene Thermal Maximum (PETM) (refs. 65,66). High-resolution (~ 1 kyr) benthic foraminiferal carbon ($\delta^{13}\text{C}_b$) and oxygen isotope records were previously generated from four ODP Sites (1262, 1263, 1265, and 1267) at the Walvis Ridge, Southeastern Atlantic and from one ODP Site (690) at Maud Rise in the Weddell Sea, Southern Ocean⁶⁶ (Supplementary Fig. S1) with paleowater depths ranging from ~ 1500 to ~ 3600 m (refs. 17,67–69). The $\delta^{18}\text{O}_b$ records of all these sites show almost identical values, suggesting that they reflect similar deep-sea conditions⁶⁶. We re-examined these sites and applied paired stable and clumped isotope analyses on the benthic foraminiferal species *Nuttallides truempyi* and *Oridorsalis umbonatus* for accurate reconstruction of deep-sea temperatures in the South Atlantic across these two hyperthermals. Overall, we find warmer deep-sea temperatures from Δ_{47} than estimates based on $\delta^{18}\text{O}_b$, which has implications for the conceptual understanding of the $\delta^{18}\text{O}_{\text{sw}}$ composition and/or pH effects that govern the oxygen isotope proxy. Based on our findings, we propose a re-evaluation of the interpretation of $\delta^{18}\text{O}_b$ records in the geological past.

Results and discussion

Stable and clumped isotope analysis. Our carbon and oxygen isotope measurements (Fig. 1) are consistent with the previously published $\delta^{13}\text{C}_b$ and $\delta^{18}\text{O}_b$ records⁶⁶. Distinct negative excursions in $\delta^{13}\text{C}_b$ (-1.4‰ and -0.8‰ , respectively) and $\delta^{18}\text{O}_b$ (-0.8‰ and -0.5‰ , respectively) characterize ETM2 and H2, showing that ETM2 is the larger event of the two. These negative $\delta^{13}\text{C}_b$ and $\delta^{18}\text{O}_b$ excursions suggest the injection of large amounts of ¹³C-depleted carbon into the climate system and elevated deep-sea temperatures, respectively^{65,66}. Limited isotope data are obtained for the peak ETM2 interval at the Walvis Ridge sites, as benthic foraminifera are rare and small-sized in the associated red clay layer, known as the Elmo horizon^{65,66}.

Due to the sporadic natural abundance of ¹³C–¹⁸O bonds within carbonate ions^{45,46}, clumped isotope analysis requires large samples to achieve high analytical precision^{54–58}, which is needed in paleoclimate reconstructions. Averaging of numerous replicate Δ_{47} measurements (>30 replicates of ~ 100 μg each) is required to mitigate large analytical uncertainty^{54–58}. The strategy of averaging Δ_{47} measurements for precise reconstruction of small temperature variability becomes especially important when sample size is limited⁷⁰. In our study, the abundance of *N. truempyi* and *O. umbonatus* is too low in the samples at all sites to take sufficient measurements for the precise reconstruction of deep-sea temperature change across ETM2 and H2. As a solution to acquire the desired precision (<3 °C at 95% Confidence Interval), we sorted the Δ_{47} measurements from all sites based on their corresponding $\delta^{18}\text{O}_b$ values and compiled three average Δ_{47} -based temperatures that represent the average background state (high $\delta^{18}\text{O}_b$), average slope (middle $\delta^{18}\text{O}_b$), and average hyperthermal peak (low $\delta^{18}\text{O}_b$) conditions across the entire

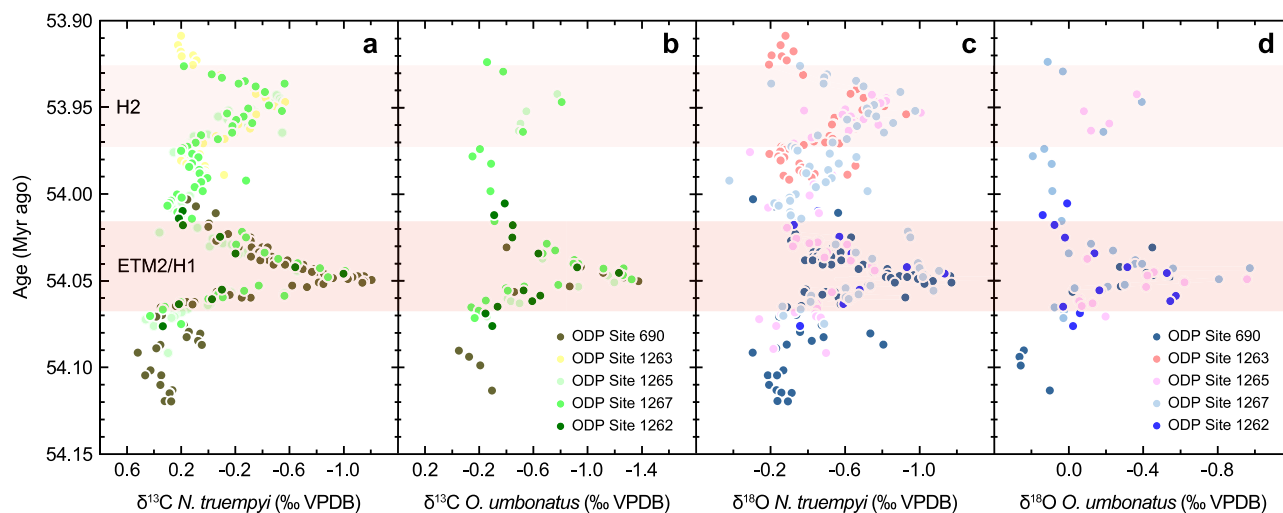


Fig. 1 South Atlantic benthic foraminiferal $\delta^{13}\text{C}$ and $\delta^{18}\text{O}$ records across ETM2 and H2. The figure shows the $\delta^{13}\text{C}$ and $\delta^{18}\text{O}$ measurements of benthic foraminifera *N. truempyi* (a and b, respectively) and *O. umbonatus* (c and d, respectively). The offsets in the stable isotopes between the two species suggest species-specific vital effects³⁰. The sites from the Walvis Ridge used for benthic foraminiferal stable and clumped isotope analysis include ODP Sites 1262, 1263, 1265, and 1267. Paleowater depth of these sites ranges from ~1500 to ~3600 m in the order 1263, 1265, 1267, 1262 (shallow to deep)^{17,67}. Maud Rise is represented by ODP Site 690 with a ~2100 m paleowater depth^{68,69}. The stable isotope data are plotted against age following the age models of Stap et al.⁶⁶ and Westerhold et al.¹²⁶.

studied period⁷⁰. Thus instead of showing deep-sea temperatures in a time series, we plotted three temperature bins that contain measurements of both the ETM2 and H2 intervals, which are representative of three different climate states. Unequal variance (Welch's) *t*-tests were performed between the 'high $\delta^{18}\text{O}_b$ ' and 'low $\delta^{18}\text{O}_b$ ' Δ_{47} measurements to determine the most optimal bin size for the background and hyperthermal temperatures⁷⁰ (Supplementary Table S1 and Fig. S2).

Deep-sea temperatures. Our Δ_{47} -based reconstruction indicates very warm deep waters with average background temperatures of 13.5 ± 1.9 °C (95% Confidence Interval) and average hyperthermal peak temperatures of 16.9 ± 2.3 °C (95% CI) (Fig. 2b; Supplementary Fig. S3 for temperatures per site). Statistically, these background and average hyperthermal peak temperature bins are significantly different from each other at 98% CI (*p*-value of 0.02). The peak temperature of ETM2 is expected to be higher than our reconstructed average of 16.9 ± 2.3 °C (95% CI). This is because the bin of the hyperthermal peak temperature combines Δ_{47} measurements of both the ETM2 and H2 events, in which ETM2 has almost twice the magnitude in $\delta^{18}\text{O}_b$ of H2 (ref. 66) (Figs. 1 and 2a). As such, this approach creates a smoothing effect in which the peak temperature of ETM2 is underestimated.

In terms of absolute values, our deep-sea temperatures from clumped isotopes are in broad agreement with benthic Mg/Ca-based records available from the Pacific, which indicate mean temperatures at 54 Ma of 15.0 or 16.3 °C with an uncertainty of ± 3.0 °C (90% CI) based on two calibrations^{32,39,40,43} (Supplementary Fig. S4). However, Mg/Ca records from the Paleocene to the early Eocene provide questionable trends in deep-sea temperature, as the Paleocene stands out to be warmer than the early Eocene, which does not become apparent from $\delta^{18}\text{O}_b$ records^{12,16} (Supplementary Fig. S4). These unexpected temperatures suggest that these records may be biased before the middle Eocene (>48 Ma) due to changing Mg/Ca_{sw} and different foraminiferal Mg/Ca-temperature sensitivity^{32,39}, which makes them less reliable.

To compare the Δ_{47} -based deep-sea temperatures with those derived from $\delta^{18}\text{O}_b$ estimates, we used the same approach as

applied in the revised Cenozoic $\delta^{18}\text{O}_b$ -based deep-sea temperature compilation by Cramer et al.³². Traditionally, it is common practice¹² to apply the classic $\delta^{18}\text{O}$ -temperature relationship of Shackleton⁷¹ based on few core top data, together with the assumption that the $\delta^{18}\text{O}$ composition of modern *Oridorsalis* is in equilibrium with the seawater composition^{72–74}. *Cibicides* is the foraminiferal genus mostly used for deep ocean reconstructions¹² and is usually corrected for seawater equilibrium since it was found that the modern genus has a 0.64‰ offset in $\delta^{18}\text{O}$ with *Oridorsalis*^{72–74}. However, more recent studies show evidence that modern *Cibicides* are actually in close isotopic equilibrium with seawater and derive a $\delta^{18}\text{O}$ -temperature relationship from this genus based on a large dataset^{75–77}. To calculate early Cenozoic deep-sea temperatures from other foraminiferal species with reference to *Cibicides*, well-documented correction factors are used to account for interspecies $\delta^{18}\text{O}_b$ offsets^{30,32}. We adjusted the *N. truempyi* and *O. umbonatus* $\delta^{18}\text{O}$ values towards *Cibicides* and subsequently calculated deep-sea temperatures from these values following Marchitto et al.⁷⁷ (Methods and Fig. 2b). For the mean $\delta^{18}\text{O}_{\text{sw}}$ of the global ocean used in $\delta^{18}\text{O}_b$ -based temperature reconstructions, we adopted a fixed value of -1 ‰ VSMOW based on the assumption of absence of ice sheets in the early Eocene²⁶.

In comparison to the $\delta^{18}\text{O}_b$ -based deep-sea temperatures of the three bins, our reconstructions from clumped isotopes are on average three degrees warmer, i.e. 13.5 ± 1.9 °C versus 10.8 ± 0.1 °C for the background, 15.0 ± 2.0 °C versus 12.0 ± 0.1 °C for the slope, and 16.9 ± 2.3 °C versus 13.6 ± 0.2 °C (all errors as 95% CI) for the average hyperthermal peak temperatures (Fig. 2b). Note that if we would instead apply the traditional $\delta^{18}\text{O}$ -temperature equation⁷¹ and assume *Oridorsalis* $\delta^{18}\text{O}$ representing equilibrium, the derived temperature differences between clumped isotopes and oxygen isotopes are larger as the $\delta^{18}\text{O}_b$ -based temperatures become ~ 1 °C cooler using that approach (Supplementary Fig. S4). The significant temperature discrepancy between Δ_{47} and $\delta^{18}\text{O}_b$ means that there is an apparent bias in the deep-sea temperatures from oxygen isotopes towards cooler values. This underestimation of temperature by $\delta^{18}\text{O}_b$ suggests that the used assumptions on non-thermal factors are incorrect.

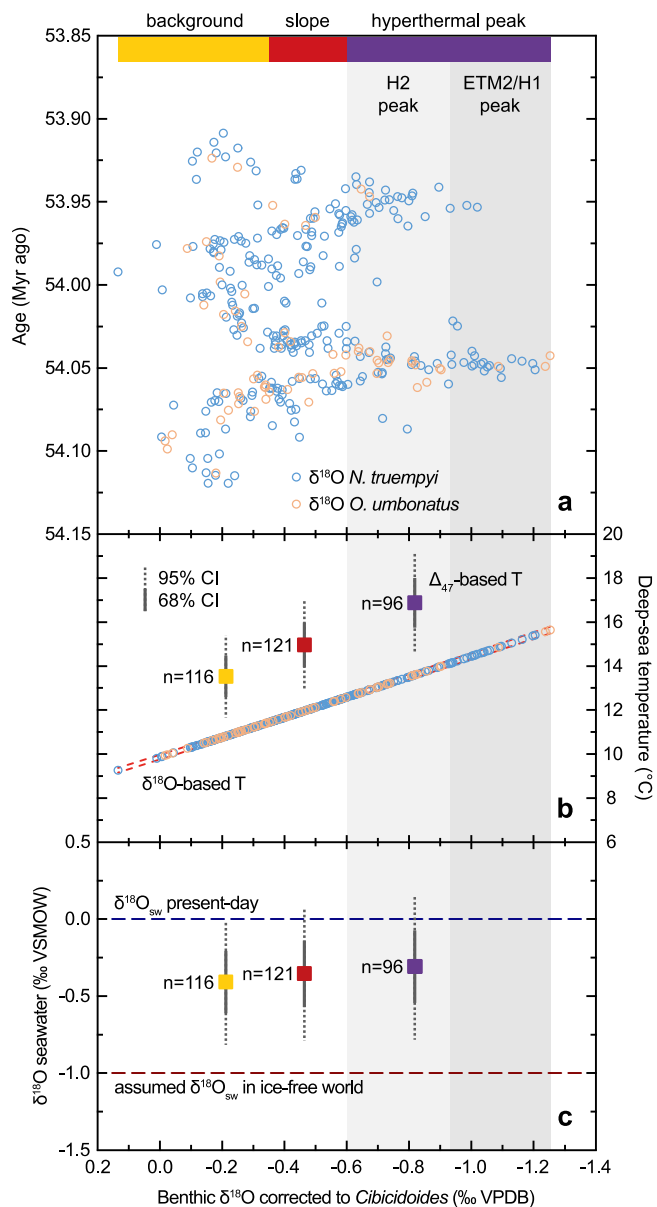


Fig. 2 Deep-sea temperatures and $\delta^{18}\text{O}$ seawater composition across ETM2–H2. **a** $\delta^{18}\text{O}_b$ values derived from *N. truempyi* and *O. umbonatus* that are corrected towards *Cibicoides* (assumed seawater equilibrium). **b** Deep-sea temperatures based on Δ_{47} and $\delta^{18}\text{O}_b$ including the number of Δ_{47} (and $\delta^{18}\text{O}_b$) measurements that are contained in the background, slope, and hyperthermal peak temperature bins. The yellow (background), red (slope), and purple (hyperthermal peak) bars indicate the range in $\delta^{18}\text{O}_b$ values corresponding to the Δ_{47} measurements that were used for compiling the three bins. The dark grey error bars on the Δ_{47} -based temperatures represent fully propagated analytical and calibration uncertainties as 68% (solid) and 95% (dashed) CI (Methods). The dashed red envelope on the $\delta^{18}\text{O}_b$ -based deep-sea temperatures displays the uncertainty (95% CI) of the $\delta^{18}\text{O}_b$ -temperature calibration of Marchitto et al.⁷⁷. Analytical uncertainty on the $\delta^{18}\text{O}_b$ -based temperatures of the three bins is very small ($\pm 0.1^\circ\text{C}$ 95% CI) and is therefore contained within the data symbols (Methods). **c** $\delta^{18}\text{O}_{\text{sw}}$ (in ‰ VSMOW) of the background, slope, and hyperthermal peak bins including uncertainties as 68% (solid) and 95% (dashed) CI. Values of $\delta^{18}\text{O}_{\text{sw}}$ were calculated using the mean Δ_{47} -based temperatures in combination with the average $\delta^{18}\text{O}_b$ values of the three bins in the $\delta^{18}\text{O}_b$ -temperature relationship of Marchitto et al.⁷⁷ (Methods). The horizontal red and blue dashed lines show the assumed $\delta^{18}\text{O}_{\text{sw}}$ value based on ice-free conditions and the present-day $\delta^{18}\text{O}_{\text{sw}}$ value, respectively.

Constraints on early Eocene $\delta^{18}\text{O}_{\text{sw}}$ composition. An important consequence of the warmer Δ_{47} -derived deep-sea temperatures is that they imply a mean value for deep water $\delta^{18}\text{O}_{\text{sw}}$ of approximately $-0.35 \pm 0.4\text{‰}$ VSMOW (95% CI), which is significantly higher than the usually assumed value (Fig. 2c). At first glance, this enriched $\delta^{18}\text{O}_{\text{sw}}$ value would suggest the presence of substantial continental ice sheets in the early Eocene. However, this hypothesis is unlikely given that subtropical temperatures and vegetation prevailed at both poles^{3,5,78–80}. Although small ephemeral ice caps might have existed on Antarctica and in the Arctic region, records of ice-rafted debris in marine sediments indicate that polar ice formation was not initiated before the middle Eocene^{81,82}. Hence, we turn to other factors that may explain a relatively high $\delta^{18}\text{O}_{\text{sw}}$ composition.

The distribution of different water masses in the early Eocene could have caused differences in the $\delta^{18}\text{O}_{\text{sw}}$ value of the ocean. The early Eocene deep Atlantic basin might have been filled with more saline waters, characterized by high $\delta^{18}\text{O}_{\text{sw}}$. Assigning exact numbers on the salinity is complicated by the fact that the salinity– $\delta^{18}\text{O}_{\text{sw}}$ relationship is not constant across the global ocean, as observed in modern water masses⁷⁶. Deep water formation is thought to have predominantly occurred in the high-latitude Southern Ocean^{83,84}. Although, saline deep waters might have formed more easily at the lower latitudes, such as the Tethys Ocean, where high evaporation would have increased salinity and hence density of the surface water^{85,86}. However, a direct implication of this situation would be that other regions of the deep ocean must have had much fresher waters (with lower $\delta^{18}\text{O}_{\text{sw}}$). Large regional salinity differences are required to meet the global seawater isotope budget and thus to balance the global ocean $\delta^{18}\text{O}_{\text{sw}}$ towards ice-free conditions. At first sight, such large heterogeneity in the ocean, i.e. large spatial differences in $\delta^{18}\text{O}_{\text{sw}}$, is difficult to reconcile with relatively small gradients in $\delta^{13}\text{C}_b$ and $\delta^{18}\text{O}_b$ that have been found between the ocean basins in the early Eocene^{20,21,87}. However, we acknowledge that similar $\delta^{18}\text{O}_b$ values across different ocean basins do not necessarily exclude the possibility that water masses would have had different properties in terms of temperature and salinity. Although speculative, it might be that warmer saltier water masses and cooler fresher water masses resulted in the same $\delta^{18}\text{O}_b$ values being recorded by the benthic foraminifera. In this situation, an intensified hydrological cycle in the Eocene hothouse may have caused increased regional salinity differences in the ocean^{78,80,88–90}, which might have enabled the formation of deep water masses with different properties.

Changes in substantial groundwater storage on land and isotope interaction between seawater and oceanic crust are factors that may have affected the $\delta^{18}\text{O}_{\text{sw}}$ composition on a global scale. Much like ice sheets, large aquifers filled with isotopically depleted water would change the $\delta^{18}\text{O}_{\text{sw}}$ towards more positive values⁹¹. It has been hypothesized that the charging and discharging of these groundwater reservoirs could explain apparent large sea level fluctuations in the hothouse climate of the Cretaceous⁹¹. However, geological evidence for large aquifer existence is not available and climate models have not yet been able to simulate increased groundwater storage in warm climates⁹². On million-year time scales, isotopic exchange of ocean water cycling through the oceanic crust at mid-ocean ridges may change through faster and slower seafloor spreading^{93,94}. The classic idea has been that seafloor spreading rates and associated volcanic activity were higher in the Cretaceous and early Eocene times, which is often used as one explanation for the high atmospheric CO_2 levels^{4,95,96}. Studies propose that an intensification of high-temperature basalt-seawater interactions (e.g. circulation of hydrothermal fluids) during faster seafloor spreading would have released more ^{18}O from the ocean crust,

enriching the seawater with heavy oxygen^{93,94}. Afterwards, low-temperature processes (e.g. submarine weathering) would have become dominant at mid-ocean ridges when spreading rates decreased. This low-temperature basalt alteration would then have preferentially removed ^{18}O from the seawater, decreasing the ice-free $\delta^{18}\text{O}_{\text{sw}}$ value towards more recent times^{93,94}. However, there is no consensus if seafloor spreading rates were truly higher in these hothouse climates, as tectonic reconstructions and model simulations find conflicting results^{97–99}. In summary, elevated $\delta^{18}\text{O}_{\text{sw}}$ in the early Eocene deep ocean can be ascribed to several factors. Our current understanding does not point towards one explanation as the most probable and a high $\delta^{18}\text{O}_{\text{sw}}$ could result from a combination of these factors as well.

Potential pH effect on $\delta^{18}\text{O}_b$ and species-specific isotope fractionation. In addition to $\delta^{18}\text{O}_{\text{sw}}$, other non-thermal factors have been considered to influence the foraminiferal $\delta^{18}\text{O}$ composition. An underestimation of $\delta^{18}\text{O}_{\text{sw}}$ may not be necessary to explain the apparent cool temperature bias of $\delta^{18}\text{O}_b$. In fact, the assumed $\delta^{18}\text{O}_{\text{sw}}$ value of -1‰ VSMOW may still be supported by our warm Δ_{47} -based deep-sea temperatures if a pH effect on the incorporation of the oxygen isotopes in the foraminiferal shell is taken into account. Boron isotope analyses on planktic foraminifera indicate that pH at the sea surface of the Eocene, which is directly linked to the high atmospheric CO_2 concentrations, was approximately 0.5 units lower than today (~ 7.7 versus ~ 8.2 , respectively)^{1,2,100}. At the moment, such absolute pH reconstructions are not available for the deep ocean. The pH at the seafloor does not necessarily follow the sea surface pH in exactly the same way, because degradation of organic matter, carbonate dissolution, and ocean circulation affect the distribution of dissolved inorganic carbon species in the deep ocean^{101–103}. Despite this, combined proxy-model and model studies suggest lower pH in the Eocene Atlantic deep ocean as well^{104–106}. Theory predicts that pH influences the oxygen isotope composition of foraminiferal calcite^{27,28}, which is confirmed in culture experiments²⁹. Decreasing pH generally causes foraminiferal $\delta^{18}\text{O}$ to increase and hence biases temperature to cooler values, but the magnitude of this effect has been found to vary between species²⁹. In theory, clumped isotopes are also affected by pH to some extent (although much less than oxygen isotopes), which would work in the same direction on the reconstructed temperatures^{47,50}. However, this pH effect on Δ_{47} has not been observed yet in experiments^{48,49}. Important to mention is that a pH effect on foraminiferal $\delta^{18}\text{O}$ has been successfully demonstrated for planktic foraminifera²⁹, yet it is uncertain whether this effect also exists in benthic foraminifera⁷⁷. Nonetheless, the underestimated early Eocene deep-sea temperatures shown by $\delta^{18}\text{O}_b$ are consistent with a scenario of highly reduced seawater pH.

Changes and uncertainties in species-specific isotope fractionation on geological time scales are also important to consider as a possible explanation for the relatively cool $\delta^{18}\text{O}_b$ -based deep-sea temperatures. While core top and deep time studies suggest that species-specific effects do not influence the Δ_{47} signal of foraminifera^{51–53,59,62}, offsets in $\delta^{18}\text{O}$ (and $\delta^{13}\text{C}$) are evident among different benthic foraminiferal species^{30,74}. These interspecies offsets in $\delta^{18}\text{O}$ also appear to change over time. For instance, a $\delta^{18}\text{O}$ offset of 0.64‰ is recorded between *Cibicidoides* and *Oridorsalis* in the late Cenozoic⁷⁴, while this offset is different in the early Cenozoic, i.e. 0.28‰ (ref. 30). These changing isotopic offsets suggest that vital effects may not have been constant over the Cenozoic because of evolutionary changes in the foraminifera³⁰. These offsets are however difficult to quantify, considering that changes in pH and its potential effect on $\delta^{18}\text{O}_b$ (that may be species-specific as well²⁹) may also have played a

role through geological time³⁰. Hence, it is complicated to establish an assumed species oxygen isotope equilibrium value in deep time with certainty. Another problem is that there seems to be no commonly accepted view on which modern benthic foraminiferal species precipitate their skeletons in equilibrium with seawater, in part because the physiological processes in the fractionation of oxygen isotopes during calcification are not well understood⁷⁷. As a consequence, conflicting methods are used in the literature to reconstruct deep-sea temperatures from Cenozoic $\delta^{18}\text{O}_b$ compilations^{12,16,32}.

Deep-sea warming during hyperthermal events. Our reconstructed background and average hyperthermal peak temperatures ($13.5 \pm 1.9\text{ °C}$ and $16.9 \pm 2.3\text{ °C}$, respectively) from clumped isotopes imply average deep-sea warming of $3.4 \pm 2.9\text{ °C}$ (95% CI) during ETM2–H2. Oxygen isotope thermometry may underestimate deep-sea temperature increase during hyperthermals when considering a pH effect on $\delta^{18}\text{O}_b$. Boron isotope measurements on planktic foraminifera from the PETM and ETM2 indicate further acidification of the sea surface of approximately -0.3 and -0.2 pH units, respectively^{107–109}. In absence of deep-sea pH proxy reconstructions, numerical models show that this drop in surface pH is propagated into the deep ocean¹⁰⁵. The effect of an even lower deep-sea pH would potentially dampen the negative $\delta^{18}\text{O}_b$ excursion of these events to about three-quarters of the original magnitude, resulting in a significant underestimation of the deep-sea warming^{29,105}. While the increase in temperature from Δ_{47} and $\delta^{18}\text{O}_b$ ($2.8 \pm 0.2\text{ °C}$ 95% CI based on the latter proxy) in our reconstructions seems to be fairly similar (Fig. 2b), we note that the temperature uncertainty in the Δ_{47} -based temperatures does allow the possibility that the true deep-sea warming is larger than indicated by $\delta^{18}\text{O}_b$. In that case, the oxygen isotopes would underestimate the temperature rise by one degree or more.

Alternatively, potential changes in deep ocean circulation during these events may also have influenced the magnitude of the $\delta^{18}\text{O}_b$ excursion, as these circulation changes would have affected $\delta^{18}\text{O}_{\text{sw}}$ of the deep Atlantic. Changes in grain size and benthic faunal assemblages from Atlantic sites are interpreted to indicate a switch in the Atlantic circulation during ETM2 (refs. 110,111). If such circulation changes were accompanied by an increase in salinity (and hence higher $\delta^{18}\text{O}_{\text{sw}}$) of deep water masses, this would represent an alternative mechanism that causes an apparent $\delta^{18}\text{O}_b$ underestimation of the hyperthermal deep-sea warming. Future efforts in reconstructing pH of the early Eocene deep ocean, investigating pH effects on benthic foraminiferal $\delta^{18}\text{O}$, development of salinity proxies^{112,113}, as well as more Eocene deep-sea temperature reconstructions from clumped isotopes are needed to provide better constraints on the effects of pH and salinity on $\delta^{18}\text{O}_b$ records.

Hyperthermal deep-sea temperature reconstructions based on Mg/Ca are currently only available for the PETM and indicate $4\text{--}5\text{ °C}$ warming³¹. A direct comparison of the magnitude of negative $\delta^{18}\text{O}_b$ excursions shows that the average ETM2–H2 excursion (0.6‰) is about one-quarter the size of that of the PETM ($\sim 2.5\text{‰}$) (refs. 65,66,114). In this respect, the average deep-sea warming of $3.4 \pm 2.9\text{ °C}$ (95% CI) that we estimate for ETM2–H2 from clumped isotopes is larger than the warming one would expect when taking into account the recorded PETM temperature rise from Mg/Ca. This discrepancy implies that either the current Mg/Ca-based temperatures largely underestimate the deep-sea warming during the PETM or that the relative magnitude of the $\delta^{18}\text{O}_b$ excursions between ETM2–H2 and PETM cannot be simply extrapolated in terms of temperature.

Secular changes in Mg/Ca_{sw} are likely to act on much longer time scales than hyperthermal variability³³. An underestimation of hyperthermal deep-sea temperature warming by Mg/Ca may result from a lowering of the Mg/Ca-temperature sensitivity at low Mg/Ca_{sw} values in the early Eocene^{37,44}. However, effects of much lower seawater pH on foraminiferal Mg/Ca may act in the opposite direction on the reconstructed magnitude of temperature change and might therefore cancel out the effect of a lower Mg/Ca-temperature sensitivity⁴⁴. The relative importance of these two factors is however uncertain, making it difficult to constrain to which extent they balance each other out⁴⁴.

Alternatively, Mg/Ca-based deep-sea warming of the PETM may be accurate if the ETM2–H2 and PETM were characterized by similar magnitudes of deep-sea warming despite their different $\delta^{18}\text{O}_b$ excursions. The large negative $\delta^{18}\text{O}_b$ excursion of the PETM might be a result of a large contribution of a decrease in $\delta^{18}\text{O}_{sw}$ caused by a circulation switch to a much fresher water mass during the event³¹. However, numerical models contradict such a scenario and instead find a reduction in deep water formation in the southern high latitudes and development of source regions in the saline surface waters of the Tethys Ocean during the PETM (refs. 85,86). Combined clumped isotope and Mg/Ca reconstructions across the PETM and/or ETM2 events are required to better assess the performance of Mg/Ca in estimating deep-sea temperature variability in the Eocene.

Conclusions and further implications. In short, our study shows that robust marine temperature reconstructions from foraminiferal oxygen isotopes, and Mg/Ca as well, can only be achieved with independent constraints on non-thermal effects. Without these constraints, the reliability of the classic reconstructions of the early Eocene^{12,16,32} should be questioned. Our findings corroborate similar findings in other periods of the Cenozoic, such as the Miocene^{62–64}. These findings warrant a revision of the traditional Cenozoic history of deep-sea temperatures that has provided us with a presumed benchmark of global climate evolution over the past 66 Myr (refs. 12,16,32).

Finally, our warmer temperatures may have implications for estimates of global mean temperatures and climate sensitivity in the early Eocene if we assume that our reconstructed South Atlantic deep-sea temperatures are representative of the global deep ocean. Available middle Eocene (~43 Ma) Atlantic Δ_{47} -based reconstructions from multiple sites indicate almost identical deep-sea temperatures between the North and South Atlantic⁶¹. Reconstructions from the other ocean basins (e.g. Pacific) are needed to further test this assumption of globally uniform deep-sea temperatures in the Eocene. Yet, if the early Eocene deep ocean was warmer on a global scale than previously thought, these warmer temperatures would result in higher estimates of global mean temperatures and climate sensitivity than previously obtained from $\delta^{18}\text{O}_b$ (refs. 7,9,15,16). Such higher estimates would be more consistent with constraints from sea surface temperature reconstructions^{2,9}. Through providing independent and accurate temperature reconstructions, clumped isotope thermometry opens up new opportunities to evaluate existing views on the homogeneity of the deep ocean over the Cenozoic^{20,21,87}.

Methods

Foraminiferal preservation and sampling. We measured stable and clumped isotopes on monospecific multi-specimen samples of *Nuttallides truempyi* and *Oridorsalis umbonatus*, which were picked from the >150 μm sediment size fraction of the samples of Stap et al.⁶⁶. Grouping Δ_{47} measurements from different benthic species to produce one temperature estimate requires the assumption of absence of foraminiferal species-specific effects on Δ_{47} , which is supported by both core top and deep time studies^{51–53,59,62}. Scanning electron microscope (SEM) images were previously generated to examine the preservation in the studied

interval and show that the foraminiferal tests are moderately altered by recrystallization (formation of secondary calcite)⁶⁶. Nevertheless, the effect of recrystallization of primary calcite on the Δ_{47} signal in benthic foraminifera is considered negligible^{61,62,115}, since this diagenesis usually occurs during early burial^{116,117}, and therefore records similar temperatures as the seafloor temperatures. Due to limiting numbers of picked foraminifera per sample, we needed to pool foraminifera from neighboring samples to obtain sufficient foraminiferal material (~25 specimens per measurement), which resulted in averaging in the depth domain. Before isotope analysis, foraminiferal samples were cleaned by removing adherent contaminants, for instance, nannofossils, organics, and clay particles. The foraminifera were gently cracked between two glass plates to enable any chamber infill to escape and subsequently ultrasonicated in deionized water at least two times for 30 seconds. The test fragments were rinsed until the suspended particles were removed (at least two times after one ultrasonication) and oven-dried at 40 °C for one night.

Clumped isotope analysis. In total, 333 successful stable and clumped isotope sample measurements were generated across the ETM2 and H2 intervals. Our analytical methods generally follow the methodology reported in previous work^{54–58}, and a more detailed description can be found in the Supplementary Methods. We measured samples of each ~70–100 μg foraminiferal material on a *Thermo Scientific Kiel IV* (Thermo Fisher Scientific, Waltham, MA, USA) carbonate preparation device coupled to a *Thermo Scientific MAT 253 Plus* mass spectrometer at Utrecht University. In addition, we measured an approximately equal number of carbonate standards. We employed three main standards (ETH-1, 2, and 3 in an approximate 1:1:5 ratio, respectively¹¹⁸), which differ in $\delta^{13}\text{C}$, $\delta^{18}\text{O}$, and Δ_{47} composition, to correct the sample measurements. Two additional check standards (IAEA-C2 and Merck) were measured in each run to monitor the long-term reproducibility of the instrument. External reproducibility (1 standard deviation) in Δ_{47} of IAEA-C2 after correction was 0.033‰. The $\delta^{13}\text{C}$ and $\delta^{18}\text{O}$ values (reported relative to the VPDB scale) of IAEA-C2 showed an external reproducibility (1 standard deviation) of 0.05‰ and 0.12‰, respectively¹¹⁹.

Temperature and $\delta^{18}\text{O}_{sw}$ calculations. As the relationship between Δ_{47} and temperature is nonlinear (Eq. (1)), we first determined three average values from the final corrected Δ_{47} measurements of the background, slope, and hyperthermal peak bins. To calculate deep-sea temperatures from these three mean Δ_{47} values, we employed a recent foraminiferal-based calibration⁵³, recalculated to the Inter-Carbon Dioxide Equilibrium Scale (I-CDES) in Meinicke et al.¹²⁰ using the recently updated values of the carbonate standards:⁵⁵

$$\Delta_{47}(\text{I-CDES}_{90^\circ\text{C}}) = (0.0397 \pm 0.0011) \times 10^6 / T^2 + (0.1518 \pm 0.0128) \quad (1)$$

in which temperature is given in K. This Δ_{47} -temperature relationship represents a composite of previously published foraminiferal-based calibrations^{51,52} with new foraminiferal data⁵³ and has a larger data density in the range of ocean temperatures compared to other calibrations. Within uncertainty, this regression is indistinguishable from calibrations based on inorganic calcite^{54,121,122}.

Calculation of the $\delta^{18}\text{O}_b$ -based deep-sea temperatures follows the approach that is used in the reconstruction of Cramer et al.³² (see discussion in Cramer et al.³² and Marchitto et al.⁷⁷). First, we converted $\delta^{18}\text{O}$ of *N. truempyi* and *O. umbonatus* towards *Cibicides* values for assumed seawater equilibrium using the correction factors from Katz et al.³⁰ [$\delta^{18}\text{O}_{\text{Cib}} = (\delta^{18}\text{O}_{\text{Nutt}} + 0.10) / 0.89$ and $\delta^{18}\text{O}_{\text{Cib}} = \delta^{18}\text{O}_{\text{Orid}} - 0.28$]. Subsequently, deep-sea temperatures were determined following the $\delta^{18}\text{O}$ -temperature relationship of *Cibicides*. In our study, we applied the improved calibration for this genus of Marchitto et al.⁷⁷ (Eq. (2)), which is based on a large dataset existing of both previous and new core top measurements:

$$\delta^{18}\text{O}_b(\text{‰ VPDB}) - \delta^{18}\text{O}_{sw}(\text{‰ VSMOW}) + 0.27 = (-0.245 \pm 0.005) \times T + (0.0011 \pm 0.0002) \times T^2 + (3.58 \pm 0.02) \quad (2)$$

whereby temperature is represented in °C. We used a fixed value of –1‰ VSMOW for the mean $\delta^{18}\text{O}_{sw}$ representing ice-free conditions²⁶. This quadratic regression shows good agreement with the regression of Kim & O’Neil¹²³, which is based on inorganic calcite precipitated between 10 and 40 °C (refs. 75,123).

Finally, we calculated $\delta^{18}\text{O}_{sw}$ for the background, slope, and hyperthermal bins, which allows for testing the traditional assumptions on $\delta^{18}\text{O}_{sw}$ in an ice-free world. In Eq. (2), we used the average $\delta^{18}\text{O}_b$ (corrected to *Cibicides*) values of the three climate states in combination with the mean Δ_{47} -based temperatures to calculate the three corresponding $\delta^{18}\text{O}_{sw}$ values.

Uncertainties and error propagation. For our data representation and visualization, we present uncertainties on the three average Δ_{47} -based temperatures and calculated $\delta^{18}\text{O}_{sw}$ values as 68% and 95% CI. For the Δ_{47} -based temperatures, these error bars represent combined analytical (spread of the group of Δ_{47} measurements) and calibration uncertainties. To propagate uncertainties in the Δ_{47} -based temperatures, one must first know the covariance of the slope and intercept of the Δ_{47} -temperature calibration of Meinicke et al.⁵³ (recalculated in Meinicke et al.¹²⁰), as the slope and intercept of the regression line are dependent on each other. Niklas Meinicke calculated 100,000 regression slope-intercept pairs from the recalculated calibration dataset using a York bootstrap fit, similarly as performed in Meinicke

et al.⁵³ for the original calibration^{53,124}. Using these values, we calculated the covariance between the calibration slope and intercept and subsequently propagated the analytical and calibration uncertainties into Δ_{47} -based temperature using provided Matlab scripts (Supplementary Data 3 and acknowledgements). The temperature error propagation follows the approach of Huntington et al.¹²⁵, which is based on standard error propagation formulas for correlated Gaussian errors (for a detailed explanation of the math see supporting information of Huntington et al.¹²⁵). Most of the uncertainty in the Δ_{47} -based temperatures is due to the analytical precision of the measurements and only a very small part comes from calibration uncertainty (~6% in our error bars)^{51,63,125}. To determine uncertainties in the calculated $\delta^{18}\text{O}_{\text{sw}}$, we used the Δ_{47} -based temperatures at 68% and 95% CI in Eq. (2) to focus on the uncertainty that is derived from the precision of the Δ_{47} measurements, as this is the main contributor to the uncertainty in $\delta^{18}\text{O}_{\text{sw}}$.

Regarding the temperatures from $\delta^{18}\text{O}_{\text{b}}$, analytical uncertainties on the temperatures of the three bins are very small (± 0.1 °C 95% CI) in comparison to Δ_{47} and hence fall within the plot symbols (Fig. 2b). The dashed red envelope in Fig. 2b represents the uncertainty (95% CI) of the $\delta^{18}\text{O}$ -temperature calibration of Marchitto et al.⁷⁷. In the main text, we mention uncertainties on $\delta^{18}\text{O}_{\text{b}}$ -based temperatures of the three bins as combined analytical and calibration uncertainties (in 95% CI).

Data availability

The raw and final isotope data of samples and standards used for correction are published on the EarthChem database (<https://doi.org/10.26022/IEDA/112196>) (ref. 119). In addition, the online Supplementary information accompanying this article contains the following Supplementary Data files:

- Supplementary Data 1: Final sample stable and clumped isotope data and calculated temperatures
- Supplementary Data 2: Results of unequal variance (Welch's) t-tests for optimal Δ_{47} bin sizes
- Supplementary Data 3: Matlab scripts and output files for Δ_{47} error propagation

Code availability

Matlab scripts and output files used to propagate analytical and calibration uncertainties on the Δ_{47} -based temperatures are provided in Supplementary Data 3 of the Supplementary information. The authors of these files are mentioned in the acknowledgements.

Received: 23 August 2021; Accepted: 20 January 2022;

Published online: 24 February 2022

References

1. Anagnostou, E. et al. Changing atmospheric CO₂ concentration was the primary driver of early Cenozoic climate. *Nature* **533**, 380–384 (2016).
2. Anagnostou, E. et al. Proxy evidence for state-dependence of climate sensitivity in the Eocene greenhouse. *Nat. Commun.* **11**, 1–9 (2020).
3. Sluijs, A. et al. Subtropical Arctic Ocean temperatures during the Palaeocene/Eocene Thermal Maximum. *Nature* **441**, 610–613 (2006).
4. Zachos, J. C., Dickens, G. R. & Zeebe, R. E. An early Cenozoic perspective on greenhouse warming and carbon-cycle dynamics. *Nature* **451**, 279–283 (2008).
5. Bijl, P. K. et al. Early Palaeogene temperature evolution of the southwest Pacific Ocean. *Nature* **461**, 776–779 (2009).
6. Cramwinckel, M. J. et al. Synchronous tropical and polar temperature evolution in the Eocene. *Nature* **559**, 382–386 (2018).
7. Burke, K. D. et al. Pliocene and Eocene provide best analogs for near-future climates. *Proc. Natl Acad. Sci. USA* **115**, 13288–13293 (2018).
8. Hollis, C. J. et al. The DeepMIP contribution to PMIP4: methodologies for selection, compilation and analysis of latest Paleocene and early Eocene climate proxy data, incorporating version 0.1 of the DeepMIP database. *Geosci. Model Dev* **12**, 3149–3206 (2019).
9. Inglis, G. N. et al. Global mean surface temperature and climate sensitivity of the early Eocene Climatic Optimum (EECO), Paleocene–Eocene Thermal Maximum (PETM), and latest Paleocene. *Clim. Past* **16**, 1953–1968 (2020).
10. Lunt, D. J. et al. DeepMIP: model intercomparison of early Eocene climatic optimum (EECO) large-scale climate features and comparison with proxy data. *Clim. Past* **17**, 203–227 (2021).
11. Lear, C. H., Elderfield, H. & Wilson, P. A. Cenozoic deep-sea temperatures and global ice volumes from Mg/Ca in benthic foraminiferal calcite. *Science* **287**, 269–272 (2000).
12. Zachos, J., Pagani, M., Sloan, L., Thomas, E. & Billups, K. Trends, rhythms, and aberrations in global climate 65 Ma to present. *Science* **292**, 686–693 (2001).
13. Valdes, P. J., Scotese, C. R. & Lunt, D. J. Deep ocean temperatures through time. *Clim. Past* **17**, 1483–1506 (2021).
14. PALAEOSENS Project Members. Making sense of palaeoclimate sensitivity. *Nature* **491**, 683–691 (2012).
15. Hansen, J., Sato, M., Russell, G. & Kharecha, P. Climate sensitivity, sea level and atmospheric carbon dioxide. *Philos. Trans. R. Soc. A* **371**, 20120294 (2013).
16. Westerhold, T. et al. An astronomically dated record of Earth's climate and its predictability over the last 66 million years. *Science* **369**, 1383–1387 (2020).
17. Zachos, J. C. et al. Rapid acidification of the ocean during the Paleocene–Eocene Thermal Maximum. *Science* **308**, 1611–1615 (2005).
18. Sexton, P. F. et al. Eocene global warming events driven by ventilation of oceanic dissolved organic carbon. *Nature* **471**, 349–352 (2011).
19. Turner, S. K., Sexton, P. F., Charles, C. D. & Norris, R. D. Persistence of carbon release events through the peak of early Eocene global warmth. *Nat. Geosci.* **7**, 748–751 (2014).
20. Lauretano, V., Zachos, J. C. & Lourens, L. J. Orbitally paced carbon and deep-sea temperature changes at the peak of the Early Eocene Climatic Optimum. *Paleoceanogr. Paleoclimatol.* **33**, 1050–1065 (2018).
21. Westerhold, T., Röhl, U., Donner, B. & Zachos, J. C. Global extent of early Eocene hyperthermal events: a new Pacific benthic foraminiferal isotope record from Shatsky Rise (ODP Site 1209). *Paleoceanogr. Paleoclimatol.* **33**, 626–642 (2018).
22. Dickens, G. R., O'Neil, J. R., Rea, D. K. & Owen, R. M. Dissociation of oceanic methane hydrate as a cause of the carbon isotope excursion at the end of the Paleocene. *Paleoceanography* **10**, 965–971 (1995).
23. DeConto, R. M. et al. Past extreme warming events linked to massive carbon release from thawing permafrost. *Nature* **484**, 87–91 (2012).
24. Ravelo, A. C. & Hillaire-Marcel, C. The use of oxygen and carbon isotopes of foraminifera in paleoceanography. In *Proxies in Late Cenozoic Paleoceanography. Developments in Marine Geology* Vol. 1 (eds. de Vernal, A. & Hillaire-Marcel, C.) 735–764 (Elsevier, 2007).
25. Pearson, P. N. Oxygen isotopes in foraminifera: Overview and historical review. In *Reconstructing Earth's Deep-Time Climate—The State of the Art in 2012. The Paleontological Society Papers* Vol. 18 (eds. Ivany, L. C. & Huber, B. T.) 1–38 (The Paleontological Society, 2012).
26. Shackleton, N. J. Paleogene stable isotope events. *Palaeogeogr. Palaeoclimatol. Palaeoecol.* **57**, 91–102 (1986).
27. Zeebe, R. E. An explanation of the effect of seawater carbonate concentration on foraminiferal oxygen isotopes. *Geochim. Cosmochim. Acta* **63**, 2001–2007 (1999).
28. Zeebe, R. E. Seawater pH and isotopic paleotemperatures of Cretaceous oceans. *Palaeogeogr. Palaeoclimatol. Palaeoecol.* **170**, 49–57 (2001).
29. Spero, H. J., Bijma, J., Lea, D. W. & Bemis, B. E. Effect of seawater carbonate concentration on foraminiferal carbon and oxygen isotopes. *Nature* **390**, 497–500 (1997).
30. Katz, M. E. et al. Early Cenozoic benthic foraminiferal isotopes: species reliability and interspecies correction factors. *Paleoceanography* **18**, 1024 (2003).
31. Tripati, A. & Elderfield, H. Deep-sea temperature and circulation changes at the Paleocene–Eocene Thermal Maximum. *Science* **308**, 1894–1898 (2005).
32. Cramer, B. S., Miller, K. G., Barrett, P. J. & Wright, J. D. Late Cretaceous–Neogene trends in deep ocean temperature and continental ice volume: Reconciling records of benthic foraminiferal geochemistry ($\delta^{18}\text{O}$ and Mg/Ca) with sea level history. *J. Geophys. Res. Oceans* **116**, C12023 (2011).
33. Evans, D. & Müller, W. Deep time foraminifera Mg/Ca paleothermometry: nonlinear correction for secular change in seawater Mg/Ca. *Paleoceanography* **27**, PA4205 (2012).
34. Coggon, R. M., Teagle, D. A., Smith-Duque, C. E., Alt, J. C. & Cooper, M. J. Reconstructing past seawater Mg/Ca and Sr/Ca from mid-ocean ridge flank calcium carbonate veins. *Science* **327**, 1114–1117 (2010).
35. Gothmann, A. M. et al. Fossil corals as an archive of secular variations in seawater chemistry since the Mesozoic. *Geochim. Cosmochim. Acta* **160**, 188–208 (2015).
36. Lear, C. H. et al. Neogene ice volume and ocean temperatures: Insights from infaunal foraminiferal Mg/Ca paleothermometry. *Paleoceanography* **30**, 1437–1454 (2015).
37. Evans, D., Brierley, C., Raymo, M. E., Erez, J. & Müller, W. Planktic foraminifera shell chemistry response to seawater chemistry: Pliocene–Pleistocene seawater Mg/Ca, temperature and sea level change. *Earth Planet. Sci. Lett.* **438**, 139–148 (2016).
38. Evans, D. et al. Eocene greenhouse climate revealed by coupled clumped isotope–Mg/Ca thermometry. *Proc. Natl Acad. Sci. USA* **115**, 1174–1179 (2018).
39. Miller, K. G. et al. Cenozoic sea-level and cryospheric evolution from deep-sea geochemical and continental margin records. *Sci. Adv.* **6**, eaaz1346 (2020).
40. Rathmann, S., Hess, S., Kuhnert, H. & Mulitza, S. Mg/Ca ratios of the benthic foraminifera *Oridorsalis umbonatus* obtained by laser ablation from core top sediments: Relationship to bottom water temperature. *Geochem. Geophys. Geosyst.* **5**, Q12013 (2004).

41. Elderfield, H., Yu, J., Anand, P., Kiefer, T. & Nyland, B. Calibrations for benthic foraminiferal Mg/Ca paleothermometry and the carbonate ion hypothesis. *Earth Planet. Sci. Lett.* **250**, 633–649 (2006).
42. Bryan, S. P. & Marchitto, T. M. Mg/Ca-temperature proxy in benthic foraminifera: New calibrations from the Florida Straits and a hypothesis regarding Mg/Li. *Paleoceanography* **23**, PA2220 (2008).
43. Lear, C. H., Mawbey, E. M. & Rosenthal, Y. Cenozoic benthic foraminiferal Mg/Ca and Li/Ca records: Toward unlocking temperatures and saturation states. *Paleoceanography* **25**, PA4215 (2010).
44. Evans, D., Wade, B. S., Henehan, M., Erez, J. & Müller, W. Revisiting carbonate chemistry controls on planktic foraminifera Mg/Ca: implications for sea surface temperature and hydrology shifts over the Paleocene–Eocene Thermal Maximum and Eocene–Oligocene transition. *Clim. Past* **12**, 819–835 (2016).
45. Ghosh, P. et al. ^{13}C – ^{18}O bonds in carbonate minerals: a new kind of paleothermometer. *Geochim. Cosmochim. Acta* **70**, 1439–1456 (2006).
46. Eiler, J. M. “Clumped-isotope” geochemistry—the study of naturally-occurring, multiply-substituted isotopologues. *Earth Planet. Sci. Lett.* **262**, 309–327 (2007).
47. Hill, P. S., Tripati, A. K. & Schauble, E. A. Theoretical constraints on the effects of pH, salinity, and temperature on clumped isotope signatures of dissolved inorganic carbon species and precipitating carbonate minerals. *Geochim. Cosmochim. Acta* **125**, 610–652 (2014).
48. Tang, J., Dietzel, M., Fernandez, A., Tripati, A. K. & Rosenheim, B. E. Evaluation of kinetic effects on clumped isotope fractionation (Δ_{47}) during inorganic calcite precipitation. *Geochim. Cosmochim. Acta* **134**, 120–136 (2014).
49. Tripati, A. K. et al. Beyond temperature: Clumped isotope signatures in dissolved inorganic carbon species and the influence of solution chemistry on carbonate mineral composition. *Geochim. Cosmochim. Acta* **166**, 344–371 (2015).
50. Guo, W. Kinetic clumped isotope fractionation in the DIC–H₂O–CO₂ system: patterns, controls, and implications. *Geochim. Cosmochim. Acta* **268**, 230–257 (2020).
51. Peral, M. et al. Updated calibration of the clumped isotope thermometer in planktonic and benthic foraminifera. *Geochim. Cosmochim. Acta* **239**, 1–16 (2018).
52. Piasecki, A. et al. Application of clumped isotope thermometry to benthic foraminifera. *Geochem. Geophys. Geosyst.* **20**, 2082–2090 (2019).
53. Meinicke, N. et al. A robust calibration of the clumped isotopes to temperature relationship for foraminifera. *Geochim. Cosmochim. Acta* **270**, 160–183 (2020).
54. Bernasconi, S. M. et al. Reducing uncertainties in carbonate clumped isotope analysis through consistent carbonate-based standardization. *Geochem. Geophys. Geosyst.* **19**, 2895–2914 (2018).
55. Bernasconi, S. M. et al. InterCarb: A community effort to improve interlaboratory standardization of the carbonate clumped isotope thermometer using carbonate standards. *Geochem. Geophys. Geosyst.* **22**, e2020GC009588 (2021).
56. Hu, B. et al. A modified procedure for gas-source isotope ratio mass spectrometry: the long-integration dual-inlet (LIDI) methodology and implications for clumped isotope measurements. *Rapid Commun. Mass Spectrom.* **28**, 1413–1425 (2014).
57. Meckler, A. N., Ziegler, M., Millán, M. I., Breitenbach, S. F. & Bernasconi, S. M. Long-term performance of the Kiel carbonate device with a new correction scheme for clumped isotope measurements. *Rapid Commun. Mass Spectrom.* **28**, 1705–1715 (2014).
58. Müller, I. A. et al. Carbonate clumped isotope analyses with the long-integration dual-inlet (LIDI) workflow: scratching at the lower sample weight boundaries. *Rapid Commun. Mass Spectrom.* **31**, 1057–1066 (2017).
59. Thornalley, D. J. et al. A warm and poorly ventilated deep Arctic Mediterranean during the last glacial period. *Science* **349**, 706–710 (2015).
60. Leutert, T. J., Auderset, A., Martínez-García, A., Modestou, S. & Meckler, A. N. Coupled Southern Ocean cooling and Antarctic ice sheet expansion during the middle Miocene. *Nat. Geosci.* **13**, 634–639 (2020).
61. Leutert, T. J. et al. Sensitivity of clumped isotope temperatures in fossil benthic and planktic foraminifera to diagenetic alteration. *Geochim. Cosmochim. Acta* **257**, 354–372 (2019).
62. Modestou, S. E., Leutert, T. J., Fernandez, A., Lear, C. H. & Meckler, A. N. Warm middle Miocene Indian Ocean bottom water temperatures: comparison of clumped isotope and Mg/Ca-based estimates. *Paleoceanogr. Paleoclimatol.* **35**, e2020PA003927 (2020).
63. Leutert, T. J., Modestou, S., Bernasconi, S. M. & Meckler, A. N. Southern Ocean bottom-water cooling and ice sheet expansion during the middle Miocene climate transition. *Clim. Past* **17**, 2255–2271 (2021).
64. Evans, D. Deep heat: proxies, Miocene ice, and an end in sight for paleoclimate paradoxes? *Paleoceanogr. Paleoclimatol.* **36**, e2020PA004174 (2021).
65. Lourens, L. J. et al. Astronomical pacing of late Palaeocene to early Eocene global warming events. *Nature* **435**, 1083–1087 (2005).
66. Stap, L. et al. High-resolution deep-sea carbon and oxygen isotope records of Eocene Thermal Maximum 2 and H2. *Geology* **38**, 607–610 (2010).
67. Zachos, J. C. et al. Early Cenozoic extreme climates: Walvis Ridge transect. *Proc. ODP Init. Rep.* **208**, 1–112 (2004).
68. Thomas, E. Late Cretaceous through Neogene deep-sea benthic foraminifera (Maud Rise, Weddell Sea, Antarctica). *Proc. ODP Sci. Res.* **113**, 571–594 (1990).
69. Kennett, J. P. & Stott, L. D. Abrupt deep-sea warming, palaeoceanographic changes and benthic extinctions at the end of the Palaeocene. *Nature* **353**, 225–229 (1991).
70. de Winter, N. J., Agterhuis, T. & Ziegler, M. Optimizing sampling strategies in high-resolution paleoclimate records. *Clim. Past* **17**, 1315–1340 (2021).
71. Shackleton, N. J. Attainment of isotopic equilibrium between ocean water and the benthonic foraminifera genus *Uvigerina*: Isotopic changes in the ocean during the last glacial. *Colloq. Int. Cent. Natl. Rech. Sci.* **219**, 203–209 (1974).
72. Graham, D. W., Corliss, B. H., Bender, M. L. & Keigwin, L. D. Jr Carbon and oxygen isotopic disequilibria of recent deep-sea benthic foraminifera. *Mar. Micropaleontol.* **6**, 483–497 (1981).
73. Shackleton, N. J., Hall, M. A. & Boersma, A. Oxygen and carbon isotope data from Leg 74 foraminifera. *Init. Rep. DSDP 74*, 599–612 (1984).
74. Shackleton, N. J. & Hall, M. A. The late Miocene stable isotope record, Site 926. *Proc. ODP Sci. Res.* **154**, 367–373 (1997).
75. Bemis, B. E., Spero, H. J., Bijma, J. & Lea, D. W. Reevaluation of the oxygen isotopic composition of planktonic foraminifera: Experimental results and revised paleotemperature equations. *Paleoceanography* **13**, 150–160 (1998).
76. Lynch-Stieglitz, J., Curry, W. B. & Slowey, N. A. Geostrophic transport estimate for the Florida Current from the oxygen isotope composition of benthic foraminifera. *Paleoceanography* **14**, 360–373 (1999).
77. Marchitto, T. M. et al. Improved oxygen isotope temperature calibrations for cosmopolitan benthic foraminifera. *Geochim. Cosmochim. Acta* **130**, 1–11 (2014).
78. Sluijs, A. et al. Warm and wet conditions in the Arctic region during Eocene Thermal Maximum 2. *Nat. Geosci.* **2**, 777–780 (2009).
79. Pross, J. et al. Persistent near-tropical warmth on the Antarctic continent during the early Eocene epoch. *Nature* **488**, 73–77 (2012).
80. Willard, D. A. et al. Arctic vegetation, temperature, and hydrology during Early Eocene transient global warming events. *Glob. Planet. Change* **178**, 139–152 (2019).
81. Stickley, C. E. et al. Evidence for middle Eocene Arctic sea ice from diatoms and ice-rafted debris. *Nature* **460**, 376–379 (2009).
82. Tripati, A. & Darby, D. Evidence for ephemeral middle Eocene to early Oligocene Greenland glacial ice and pan-Arctic sea ice. *Nat. Commun.* **9**, 1–11 (2018).
83. Batenburg, S. J. et al. Major intensification of Atlantic overturning circulation at the onset of Paleogene greenhouse warmth. *Nat. Commun.* **9**, 1–8 (2018).
84. Zhang, Y. et al. Early Eocene vigorous ocean overturning and its contribution to a warm Southern Ocean. *Clim. Past* **16**, 1263–1283 (2020).
85. Lunt, D. J. et al. CO₂-driven ocean circulation changes as an amplifier of Paleocene-Eocene Thermal Maximum hydrate destabilization. *Geology* **38**, 875–878 (2010).
86. Cope, J. T. & Winguth, A. On the sensitivity of ocean circulation to arctic freshwater input during the Paleocene/Eocene Thermal Maximum. *Palaeogeogr. Palaeoclimatol. Palaeoecol.* **306**, 82–94 (2011).
87. Cramer, B. S., Toggweiler, J. R., Wright, J. D., Katz, M. E. & Miller, K. G. Ocean overturning since the Late Cretaceous: Inferences from a new benthic foraminiferal isotope compilation. *Paleoceanography* **24**, PA4216 (2009).
88. Krishnan, S., Pagani, M., Huber, M. & Sluijs, A. High latitude hydrological changes during the Eocene Thermal Maximum 2. *Earth Planet. Sci. Lett.* **404**, 167–177 (2014).
89. Harper, D. T. et al. Subtropical sea-surface warming and increased salinity during Eocene Thermal Maximum 2. *Geology* **46**, 187–190 (2018).
90. Zhu, J. et al. Simulation of early Eocene water isotopes using an Earth system model and its implication for past climate reconstruction. *Earth Planet. Sci. Lett.* **537**, 116164 (2020).
91. Sames, B., Wagreich, M., Conrad, C. P. & Iqbal, S. Aquifer-eustasy as the main driver of short-term sea-level fluctuations during Cretaceous hothouse climate phases. *Geol. Soc. Lond. Spec. Publ.* **498**, 9–38 (2020).
92. Davies, A. et al. Assessing the impact of aquifer-eustasy on short-term Cretaceous sea-level. *Cretac. Res.* **112**, 104445 (2020).
93. Wallmann, K. The geological water cycle and the evolution of marine $\delta^{18}\text{O}$ values. *Geochim. Cosmochim. Acta* **65**, 2469–2485 (2001).
94. Jaffrés, J. B., Shields, G. A. & Wallmann, K. The oxygen isotope evolution of seawater: a critical review of a long-standing controversy and an improved geological water cycle model for the past 3.4 billion years. *Earth-Sci. Rev.* **83**, 83–122 (2007).

95. Larson, R. L. Geological consequences of superplumes. *Geology* **19**, 963–966 (1991).
96. Larson, R. L. Latest pulse of Earth: Evidence for a mid-Cretaceous superplume. *Geology* **19**, 547–550 (1991).
97. Conrad, C. P. & Lithgow-Bertelloni, C. Faster seafloor spreading and lithosphere production during the mid-Cenozoic. *Geology* **35**, 29–32 (2007).
98. Seton, M., Gaina, C., Müller, R. D. & Heine, C. Mid-Cretaceous seafloor spreading pulse: fact or fiction? *Geology* **37**, 687–690 (2009).
99. Coltice, N., Seton, M., Rolf, T., Müller, R. D. & Tackley, P. J. Convergence of tectonic reconstructions and mantle convection models for significant fluctuations in seafloor spreading. *Earth Planet. Sci. Lett.* **383**, 92–100 (2013).
100. Rae, J. W. et al. Atmospheric CO₂ over the past 66 million years from marine archives. *Annu. Rev. Earth Planet. Sci.* **49**, 599–631 (2021).
101. Yu, J. & Elderfield, H. Benthic foraminiferal B/Ca ratios reflect deep water carbonate saturation state. *Earth Planet. Sci. Lett.* **258**, 73–86 (2007).
102. Yu, J., Foster, G. L., Elderfield, H., Broecker, W. S. & Clark, E. An evaluation of benthic foraminiferal B/Ca and $\delta^{11}\text{B}$ for deep ocean carbonate ion and pH reconstructions. *Earth Planet. Sci. Lett.* **293**, 114–120 (2010).
103. Greenop, R. et al. A record of Neogene seawater $\delta^{11}\text{B}$ reconstructed from paired $\delta^{11}\text{B}$ analyses on benthic and planktic foraminifera. *Clim. Past* **13**, 149–170 (2017).
104. Raitzsch, M. & Hönisch, B. Cenozoic boron isotope variations in benthic foraminifers. *Geology* **41**, 591–594 (2013).
105. Uchikawa, J. & Zeebe, R. E. Examining possible effects of seawater pH decline on foraminiferal stable isotopes during the Paleocene-Eocene Thermal Maximum. *Paleoceanography* **25**, PA2216 (2010).
106. Boudreau, B. P., Middelburg, J. J., Sluijs, A. & van der Ploeg, R. Secular variations in the carbonate chemistry of the oceans over the Cenozoic. *Earth Planet. Sci. Lett.* **512**, 194–206 (2019).
107. Penman, D. E., Hönisch, B., Zeebe, R. E., Thomas, E. & Zachos, J. C. Rapid and sustained surface ocean acidification during the Paleocene-Eocene Thermal Maximum. *Paleoceanography* **29**, 357–369 (2014).
108. Babila, T. L. et al. Capturing the global signature of surface ocean acidification during the Palaeocene–Eocene Thermal Maximum. *Philos. Trans. R. Soc. A* **376**, 20170072 (2018).
109. Harper, D. T. et al. The magnitude of surface ocean acidification and carbon release during Eocene Thermal Maximum 2 (ETM-2) and the Paleocene-Eocene Thermal Maximum (PETM). *Paleoceanogr. Paleoclimatol.* **35**, e2019PA003699 (2020).
110. D’haensens, S. et al. A transient deep-sea circulation switch during Eocene Thermal Maximum 2. *Paleoceanography* **29**, 370–388 (2014).
111. Jennions, S. M., Thomas, E., Schmidt, D. N., Lunt, D. & Ridgwell, A. Changes in benthic ecosystems and ocean circulation in the Southeast Atlantic across Eocene Thermal Maximum 2. *Paleoceanography* **30**, 1059–1077 (2015).
112. Wit, J. C., de Nooijer, L. J., Wolthers, M. & Reichart, G. J. A novel salinity proxy based on Na incorporation into foraminiferal calcite. *Biogeosciences* **10**, 6375–6387 (2013).
113. Watkins, C. S., Schmidt, M. W. & Hertzberg, J. E. Calibrating *Trilobatus sacculifer* Na/Ca ratios from Atlantic core-tops as a proxy for sea surface salinity. *Paleoceanogr. Paleoclimatol.* **36**, e2021PA004277 (2021).
114. McCarren, H., Thomas, E., Hasegawa, T., Röhl, U. & Zachos, J. C. Depth dependency of the Paleocene-Eocene carbon isotope excursion: paired benthic and terrestrial biomarker records (Ocean Drilling Program Leg 208, Walvis Ridge). *Geochem. Geophys. Geosyst.* **9**, Q10008 (2008).
115. Stolper, D. A., Eiler, J. M. & Higgins, J. A. Modeling the effects of diagenesis on carbonate clumped-isotope values in deep- and shallow-water settings. *Geochim. Cosmochim. Acta* **227**, 264–291 (2018).
116. Edgar, K. M., Pälke, H. & Wilson, P. A. Testing the impact of diagenesis on the $\delta^{18}\text{O}$ and $\delta^{13}\text{C}$ of benthic foraminiferal calcite from a sediment burial depth transect in the equatorial Pacific. *Paleoceanography* **28**, 468–480 (2013).
117. Voigt, J., Hathorne, E. C., Frank, M. & Holbourn, A. Minimal influence of recrystallization on middle Miocene benthic foraminiferal stable isotope stratigraphy in the eastern equatorial Pacific. *Paleoceanography* **31**, 98–114 (2016).
118. Kocken, I. J., Müller, I. A. & Ziegler, M. Optimizing the use of carbonate standards to minimize uncertainties in clumped isotope data. *Geochem. Geophys. Geosyst.* **20**, 5565–5577 (2019).
119. Agterhuis, T., Ziegler, M., de Winter, N. J. & Lourens, L. J. *Version 1.0. Interdisciplinary Earth Data Alliance (IEDA) (data set)*. <https://doi.org/10.26022/IEDA/112196> (2022).
120. Meinicke, N., Reimi, M. A., Ravelo, A. C. & Meckler, A. N. Coupled Mg/Ca and clumped isotope measurements indicate lack of substantial mixed layer cooling in the Western Pacific Warm Pool during the last ~5 million years. *Paleoceanogr. Paleoclimatol.* **36**, e2020PA004115 (2021).
121. Kele, S. et al. Temperature dependence of oxygen- and clumped isotope fractionation in carbonates: a study of travertines and tufas in the 6–95 °C temperature range. *Geochim. Cosmochim. Acta* **168**, 172–192 (2015).
122. Anderson, N. T. et al. A unified clumped isotope thermometer calibration (0.5–1,100 °C) using carbonate-based standardization. *Geophys. Res. Lett.* **48**, e2020GL092069 (2021).
123. Kim, S. & O’Neil, J. R. Equilibrium and nonequilibrium oxygen isotope effects in synthetic carbonates. *Geochim. Cosmochim. Acta* **61**, 3461–3475 (1997).
124. York, D., Evensen, N. M., Martinez, M. L. & De Basabe Delgado, J. Unified equations for the slope, intercept, and standard errors of the best straight line. *Am. J. Phys.* **72**, 367–375 (2004).
125. Huntington, K. W. et al. Methods and limitations of ‘clumped’ CO₂ isotope (Δ_{47}) analysis by gas-source isotope ratio mass spectrometry. *J. Mass Spectrom.* **44**, 1318–1329 (2009).
126. Westerhold, T. et al. Astronomical calibration of the Ypresian timescale: implications for seafloor spreading rates and the chaotic behavior of the solar system? *Clim. Past* **13**, 1129–1152 (2017).

Acknowledgements

This research was conducted under the program of the Netherlands Earth System Science Centre (NESSC), financially supported by the Ministry of Education, Culture, and Science (OCW) of the Netherlands. M.Z. acknowledges additional funding from the Dutch Research Council (NWO), research grant 016.161.365. This work used samples and data provided by the Ocean Drilling Program (ODP). We thank the three anonymous reviewers and Sevi Modestou for their comments and suggestions that helped to improve this manuscript. We are grateful to Ilja J. Kocken (Utrecht University) for processing the raw clumped isotope data in R and Arnold E. van Dijk (Geolab of Utrecht University) for technical support in the lab. We acknowledge Alvaro Fernandez, Niklas Meinicke, Joep van Dijk, and Anna N. Meckler for sharing their Matlab scripts and output files to propagate errors. We thank Lucy Stap for picking of foraminifera.

Author contributions

T.A., M.Z., and L.J.L. designed the study. T.A. generated the stable and clumped isotope data. T.A., M.Z., N.J.W., and L.J.L. all contributed to data interpretation. T.A. wrote the article with input from all authors.

Competing interests

The authors declare no competing interests.

Additional information

Supplementary information The online version contains supplementary material available at <https://doi.org/10.1038/s43247-022-00350-8>.

Correspondence and requests for materials should be addressed to Tobias Agterhuis.

Peer review information *Communications Earth & Environment* thanks Sevasti Modestou and the other, anonymous, reviewer(s) for their contribution to the peer review of this work. Primary Handling Editor: Joe Aslin. Peer reviewer reports are available.

Reprints and permission information is available at <http://www.nature.com/reprints>

Publisher’s note Springer Nature remains neutral with regard to jurisdictional claims in published maps and institutional affiliations.



Open Access This article is licensed under a Creative Commons

Attribution 4.0 International License, which permits use, sharing, adaptation, distribution and reproduction in any medium or format, as long as you give appropriate credit to the original author(s) and the source, provide a link to the Creative Commons license, and indicate if changes were made. The images or other third party material in this article are included in the article’s Creative Commons license, unless indicated otherwise in a credit line to the material. If material is not included in the article’s Creative Commons license and your intended use is not permitted by statutory regulation or exceeds the permitted use, you will need to obtain permission directly from the copyright holder. To view a copy of this license, visit <http://creativecommons.org/licenses/by/4.0/>.

© The Author(s) 2022